AGU ADVANCING EARTH AND SPACE SCIENCE

Water Resources Research

RESEARCH ARTICLE
10.1029/2020WR029415

# Effect of Grain Shape on Quasi-Static Fluid-Fluid Displacement in Porous Media

**Zhongzheng Wang**[1,2], **Jean-Michel Pereira**[2], **and Yixiang Gan**[1,3]

[1]School of Civil Engineering, The University of Sydney, Sydney, NSW, Australia, [2]Navier, Ecole des Ponts, Université Gustave Eiffel, CNRS, Marne-la-Vallée, France, [3]The University of Sydney Nano Institute (Sydney Nano), The University of Sydney, Sydney, NSW, Australia

**Key Points:**

- A novel pore-network model algorithm is developed to probe the effect of grain shape on multiphase displacement in porous media
- Systematic simulations are conducted using the proposed algorithm across a wide range of wetting conditions and particle shapes
- Through analyzing various metrics during displacement, the results highlight the profound influence of particle shape on multiphase flow

**Supporting Information:**

Supporting Information may be found in the online version of this article.

**Correspondence to:**

Y. Gan,
yixiang.gan@sydney.edu.au

**Citation:**

Wang, Z., Pereira, J.-M., & Gan, Y. (2021). Effect of grain shape on quasi-static fluid-fluid displacement in porous media. *Water Resources Research*, *57*, e2020WR029415. https://doi.org/10.1029/2020WR029415

Received 12 DEC 2020
Accepted 15 MAR 2021



**Abstract** We study how grain shapes impact multiphase flow in porous media in the quasi-static regime using an extended pore-network model. The algorithm allows the explicit determination of different types of pore-scale instabilities and tracks the interface motion during the fluid-fluid displacement process. It also includes the volume capacitance model, such that both the evolution of capillary pressure signal and sizes of Haines jumps can be captured. Further, it considers the pinning of menisci at sharp edges of grains, through which the distribution of effective contact angles can be obtained. Simulations are carried out across a wide range of wetting conditions for different particle shapes. Our results show that the effective contact angle distribution during displacement widens as the grain becomes more angular, which consequently modifies the macroscopic fluid invasion morphology. By analyzing various characteristic metrics during displacement, including capillary pressure signal, Haines jump size distribution, and fractal dimension, our results highlight the profound influence of particle shape on the multiphase flow.

## 1. Introduction

Fluid-fluid displacement in porous media is a common phenomenon encountered in a wide range of natural and industrial processes, such as water infiltration into soil (Lipiec et al., 2006), carbon sequestration (Matter et al., 2016; Szulczewski et al., 2012), enhanced oil recovery (Blunt et al., 1993; Lake et al., 2014), and remediation of contamination in aquifer systems (Nadim et al., 2000). As indicated by the pioneering works by Lenormand et al. (1988) and Lenormand and Zarcone (1989), the multiphase displacement patterns strongly depend on the capillary number (i.e., relative strength of viscous force to capillary force) and the viscosity ratio of the two fluids, and a phase diagram including capillary fingering, viscous fingering, and stable displacement was presented. Since then, extensive efforts have been devoted to further investigation of how fluid properties, flow conditions, and topological characteristics of the porous media modify the invasion morphology (Armstrong et al., 2014; Holtzman, 2016; Hu et al., 2019; Ju et al., 2020; Rabbani et al., 2018; Wang et al., 2019; Xu et al., 2014; Yortsos et al., 1997). Specifically, both numerical and experimental works have revealed the profound influence of wettability (i.e., contact angle) in two-phase flows (Cieplak & Robbins, 1990; Crisp & Thorpe, 1948; Holtzman & Segre, 2015; Jung et al., 2016; Mason & Morrow, 1994; Primkulov et al., 2018; Purcell, 1950; Ran et al., 2018; Trojer et al., 2015; Wang et al., 2019, 2020; Zhao et al., 2016). However, the effective contact angle, as one of the key controlling factors, is often unknown prior to the displacement process due to the complex geometry of pore space. Even for chemically homogeneous porous media, a wide distribution of contact angles has been observed due to the roughness and pinning of menisci at sharp edges (AlRatrout et al., 2018; Blunt et al., 2019, 2021). Therefore, it is important to understand how particle shape affects the effective contact angles, which can consequently alter the pore-scale instability events and macroscopic invasion morphology (AlRatrout et al., 2018; Cieplak & Robbins, 1990; Geistlinger & Zulfiqar, 2020; Holtzman & Segre, 2015; Zulfiqar et al., 2020).

In the quasi-static regime of multiphase flow where capillary force dominates the displacement, various numerical approaches have been developed to supplement experiments, including Navier-Stokes equation solvers and pore-network models. The methods of the latter category have been successfully applied in the investigation of macroscopic invasion patterns due to significantly less computational cost (Blunt, 1998, 2001; Cieplak & Robbins, 1988, 1990; Holtzman, 2016; Holtzman & Segre, 2015; Hu et al., 2019; Primkulov et al., 2018). A subclass of pore-network models, the interface tracking algorithm, initially proposed by

Cieplak and Robbins (1988) and Robbins (1988, 1990) and recently extended by Primkulov et al. (2018) for consideration of corner flow, has been found successful in reproducing multiphase displacement experiments in Hele-Shaw cells (Chapuis et al., 2008; Holtzman, 2016; Holtzman & Segre, 2015; Ran et al., 2018; Trojer et al., 2015; Zhao et al., 2016). This method captures the pore-scale invasion mechanisms by taking into account the local pore geometry, including the cooperative pore-filling event, which stabilizes the invasion during imbibition (Cieplak & Robbins, 1988, 1990; Holtzman & Segre, 2015). However, up to now, this type of pore-network model is applicable to perfectly spherical particles, whereas grains with irregular shapes are prevalent in natural systems such as sand packs, and solid walls characterized by surface with sharp edges due to manufacturing limitations are encountered in microfluidics. These non-smooth surfaces can often lead to pinning of menisci during the displacement process, which results in effective contact angles deviating from the intrinsic one, altering the capillary resistance at local pore/throat. It is worth noting that surface roughness has also proven influential on the effective contact angle during the fluid-fluid displacement process (AlRatrout et al., 2018; Chen et al., 2018; Mehmani et al., 2019; Zulfiqar et al., 2020). One option to distinguish the impact from particle shape and roughness on contact angle is whether the effect is transient. Due to surface roughness, the effective contact angle can change as the liquid fills the grooves of the surface, leading to a time-dependent behavior of contact angle. This phenomenon has been extensively observed in experiments (Mishra et al., 2016; Moulinet & Bartolo, 2007; Papadopoulos et al., 2013; Sbragaglia et al., 2007; Seo et al., 2018), where the effective contact angle could be described by the Wenzel or Cassie-Baxter model, depending on the wetting states (Cassie & Baxter, 1944; Gao & Yan, 2009; Marmur, 2003; Wenzel, 1936). On the other hand, the pinning of the meniscus at sharp edges (Gibbs, 1961; Oliver et al., 1977), is a thermodynamically stable configuration. In the current study, we thus focus on the latter phenomenon in the quasi-static displacement process.

Here, we develop an extended pore-network model (called EPONM) to probe the effect of particle shape on quasi-static fluid-fluid displacement. The model incorporates the explicit determination of basic pore-scale instabilities based on the study of Cieplak and Robbins (1988, 1990). It also includes the volume capacitance model (Furuberg et al., 1996; Måløy et al., 1992), which allows us to capture both the evolution of capillary pressure signal and sizes of Haines jumps. Different from the original algorithm where the volume capacitance is a prescribed constant (Furuberg et al., 1996; Måløy et al., 1992), it is calculated based on local pore geometries without extra assumptions. More importantly, the sharp edge pinning effect is added to consider the pinning of the menisci (Gibbs, 1961; Oliver et al., 1977). Our results for different grain shapes indicate that increase in angularity leads to wider distribution of contact angles, which explains the observed greater fluctuations in capillary pressure. Besides, it is found that compared with more spherical particles, the mean capillary pressure for angular grains is greater in drainage whereas smaller in imbibition. We quantify and analyze the correlation between grain shape and size distribution of Haines jumps, interfacial length, and fractal dimension across a wide range of wetting conditions. The implications of our findings are then discussed.

## 2. Extended Pore-Network Model

To model the two-dimensional (2D) flow patterns observed in Hele-Shaw cells filled with vertical posts (Hu et al., 2019; Primkulov et al., 2018; Trojer et al., 2015; Zhao et al., 2016) with controlled particle shapes, the porous medium is represented by polygons (instead of circles in past studies) placed on 2D triangular lattice. The invading fluid is injected from the center of the simulation domain. Based on a purely geometrical extension of Young-Dupre equation (Gibbs, 1961; Oliver et al., 1977), the equilibrium state of effective contact angle $\theta$ measured within the invading fluid at the triple line follows:

$$\theta_0 \leq \theta \leq \theta_0 + (180° - \alpha), \tag{1}$$

where $\theta_0$ and $\alpha$ are the intrinsic contact angle and the angle subtended by the two surfaces forming the edge, respectively (Figure 1a). Since in this work the focus is placed on the regime of quasi-static displacement, the advancement of liquid front is governed by capillary force, and the viscous effect is ignored.

In the framework of interface tracking algorithm, the menisci move forward through two types of advancements: (1) pressure-driven events and (2) spontaneous events (relaxation). With a constant injection velocity boundary condition, the capillary pressure builds up accompanied by change in shapes in menisci,

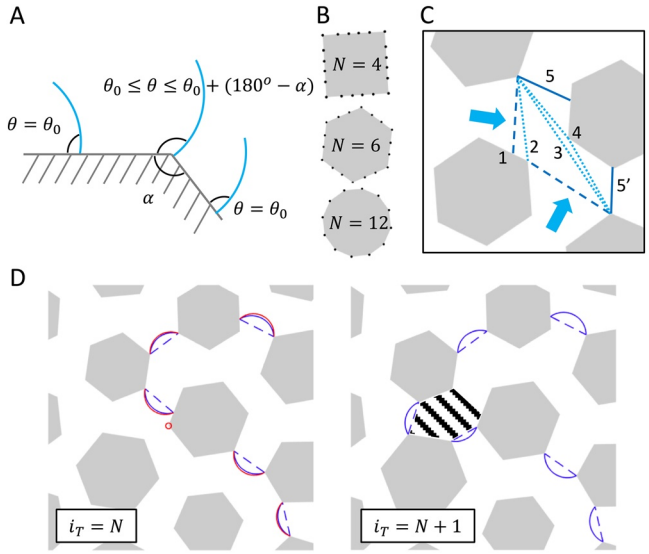


**Figure 1.** (a) Pinning of menisci at corners leads to greater effective contact angle. (b) Investigated grain shapes in this work with the different number of edges *N*. The black dots represent the mesh points. (c) Schematic showing different invasion types. {1–2, 2–3, 3–4, 4–5(5′)} correspond to {unpin, overlap, touch, unpin} events, respectively. Blue arrows mark the movement direction of menisci. (d) Snapshots of invasion morphology at two consecutive steps. Blue-solid lines represent menisci after relaxation of the previous step. Red-solid lines represent menisci at the critical state (in this case an unpin event marked by the red circle will take place). The shaded area is invaded, accompanied by retraction of menisci from red lines at $i_T = N$ to blue lines at $i_T = N + 1$.

until either the meniscus jumps toward the next mesh point due to the local contact angle being greater than the upper bound according to Equation 1 (*unpin* event), or the meniscus touches other grain, forming two new menisci (*touch* event). Regarding the fineness of the mesh, the number of mesh points needed per edge is denoted by $M = E/N$, with $E$ the effective number of mesh points per grain and $N$ the number of edges a grain has. It is found that $E = 24$ is sufficient for the studied grain shapes, leading to the corresponding number of mesh points per edge $M = 6$, 4, and 2 for square, hexagon, and dodecagon, respectively (Figure 1b). This is verified by checking both the macroscopic invasion morphology and pore-scale instability events (see the supporting information for the mesh sensitivity test). After each pressure-driven event, the newly invaded area is subtracted from the total volume capacitance (Furuberg et al., 1996; Måløy et al., 1992; area between red and blue-dashed lines in Figure 1d), from which the pressure within the invading fluid is updated according to the remaining volume capacitance, that is, redistributing the total volume back to each active meniscus assuming all are at thermodynamic equilibrium, that is, all have the same curvature. Then, potential *overlap* events and further advancement events including *unpin* and/or *touch* are checked and executed. This process is carried out until the smallest capillary resistance at the invasion front is greater than the remaining pressure within the invading fluid. Note that after each time step, trapping is checked and all menisci that belong to trapped regions are deactivated to prevent any further movement. Figure 1c shows the schematic of several advancement steps initialized by a pressure-driven *unpin* event. Figure 1d shows local snapshot of invasion morphology at two consecutive time steps. The blue-solid lines denote the menisci shape after the previous relaxation step, and red-solid lines denote the menisci shape associated with the next minimum critical capillary pressure. The flow chart of the algorithm is shown in Figure 2. More details on the algorithm, such as the calculation of critical capillary pressure, determination of instability modes, and conversion between pressure and volume can be found in the supporting information.

To investigate the effect of particle shapes, squares, hexagons, and dodecagons were chosen as representative grains with decreasing angularity (Figure 1b). The one-by-one rectangular simulation domain contains in total 7,520 particles placed on triangular lattice, corresponding to 94 columns of 80 vertically aligned grains with constant porosity of 0.5912 ± 0.0005 (see a sample packing structure in Figure 3a). Disorder is introduced by (i) inducing 10% variation in particle size with a uniform distribution and (ii) random rotation of particles in (0°, 360°). The capillary pressure signal, total injected fluid volume (area in 2D), and size of Haines jump are recorded at each step, until the invasion front reaches the boundary. Simulations were carried out for each particle shape with five randomly generated porous media under contact angles ranging from 45° to 165° with 15° increment. For displacement processes with contact angles below 45°, the 3D phenomenon corner flow starts to appear (Primkulov et al., 2018; Zhao et al., 2016), which is currently not captured in the model, and thus those processes are not covered in the present study.

A typical evolution of the invasion front until breakthrough for hexagonal grains with an intrinsic contact angle of $\theta_0 = 120°$ is shown in Figure 3a. Crimson represents the initial stage whereas yellow indicates the late times. The displacement pattern contains rather ramified structures with significant trapping, which represents the capillary fingering in drainage. Figure 3b(i) shows the evolution of the dimensionless capillary pressure calculated as the curvature $P_c^* = 1 / r^*$, with $r^*$ being the radius of the meniscus. The pressure-driven events and spontaneous events are marked by red circles and yellow cross, respectively. Clearly, multiple spontaneous events can take place following a pressure-driven event, which is a manifestation of a Haines jump. In the limit of vanishing capillary number, Haines jump can be regarded as effectively instantaneous compared with the speed of fluid injection at the inlet. Thus, after conversion from step into time, which is expressed as volume of injected area normalized by the average pore area, Figure 3b(ii) shows

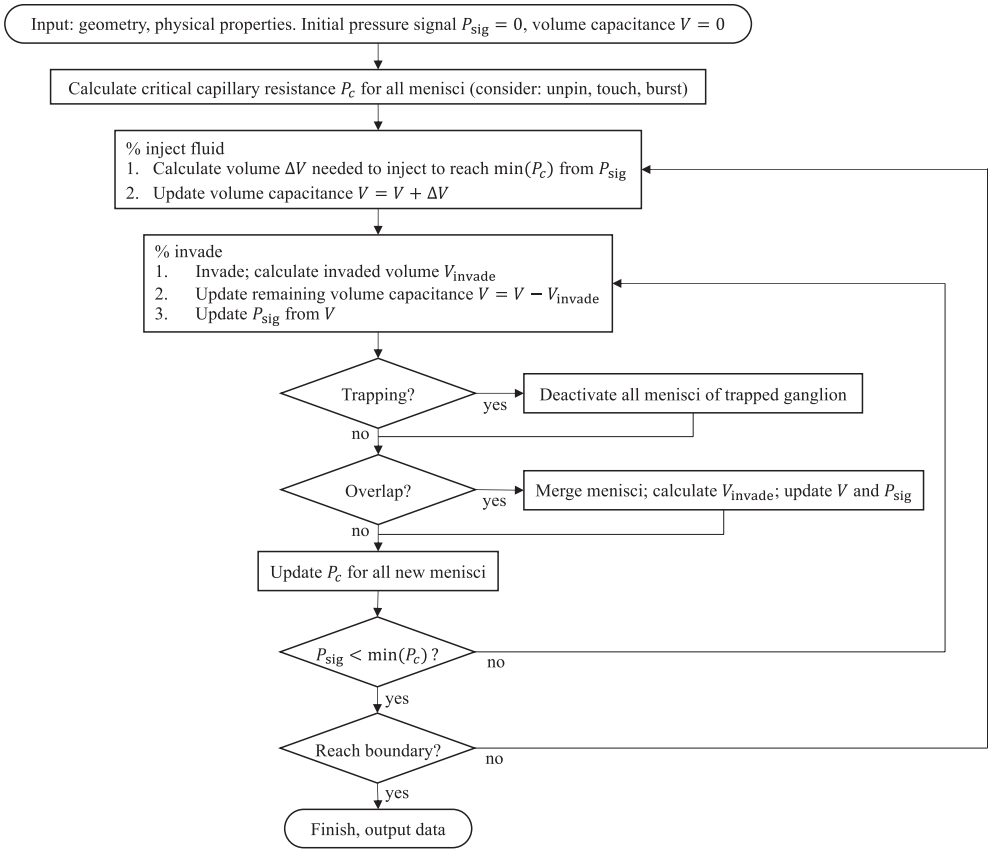


**Figure 2.** Flow chart of the pore-network model.

the pressure signal as a function of $A^*_{inj}$. The $P^*_c$ values at same invasion progress are marked by the same number in Figures 3b(i) and 3b(ii). Specifically, the processes marked by (1–2) and (2–3) represent a fast Haines jump accompanied by drop in pressure, and slow injection of invading fluid until the next critical $P^*_c$ is reached, respectively. Figure 3b(iii) shows $P^*_c$ signal for the whole simulation. Similar pressure signal signatures in a stick-slip manner have been observed in experiments at quasi-static condition (Furuberg et al., 1996; Måløy et al., 1992; Moura et al., 2020).

## 3. Results and Discussion

The phase diagram of the displacement patterns across a wide range of contact angles for different particle shapes is shown in Figure 4a. The invasion morphology for medium with dodecagons at $\theta_0 = 45°$ is compact with rather smooth front. This hexagonal shape is a direct result of the grain placement in the triangular lattice, which has been observed in the previous study (Holtzman, 2016; Lenormand, 1990). However, with increase in angularity, despite the displacement pattern is still relatively stable without trapping, the invasion front becomes more irregular, indicating a shift of the dominance of local pore geometry from lattice structure toward grain shape. The results at $\theta_0 = 60°$ demonstrate similar trend, with trapping events starting to occur for angular grains. With the increase of $\theta_0$, the displacement patterns experience a transition from compact displacement to capillary fingering. The distribution of the normalized throat size $L^*_t$, calculated as the shortest distance between adjacent grains divided by the throat size of the volume equivalent spheres, is shown in Figure 4b. Although the media have similar grain size distribution (10% variation with uniform distribution) and arrangement (placed on triangular lattice), the $L^*_t$ distribution varies drastically for different grain shapes, with wider span for more angular grains, similar to the effect from increasing topological disorder (Wang et al., 2019). Another influence of particle shape is the smaller average throat

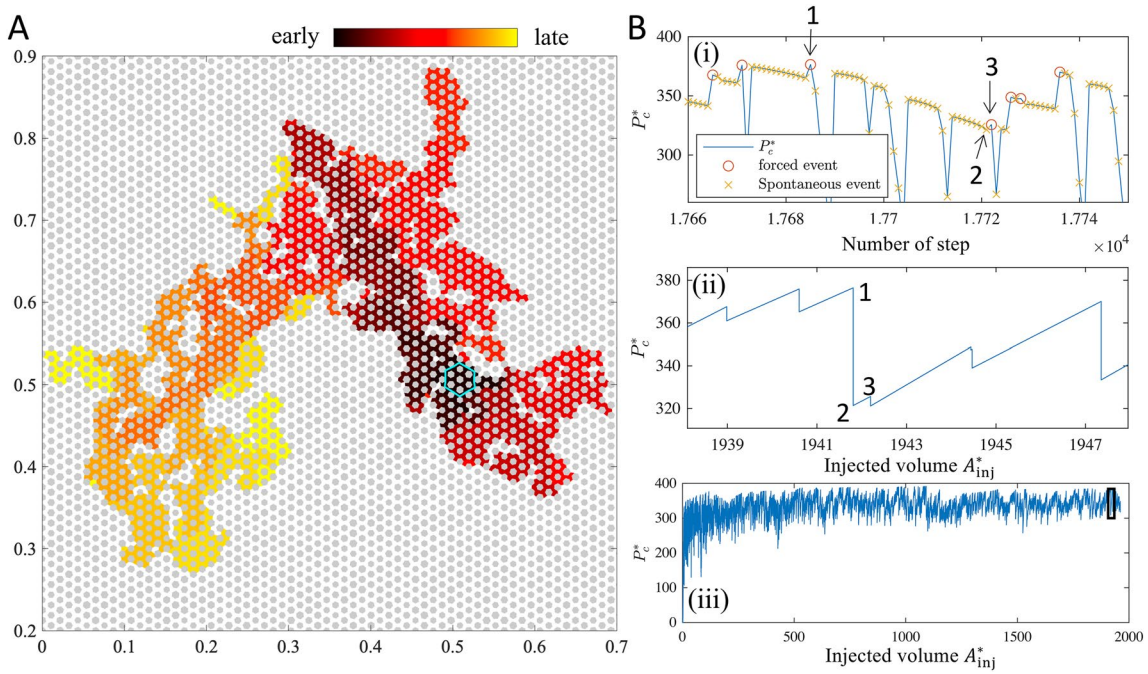


**Figure 3.** (a) Invasion morphology with hexagon grains (Number of edges $N = 6$) and $\theta_0 = 120°$. The color represents displacement patterns at different steps. The initial positions of menisci are shown as cyan lines. (b) Process of capillary pressure signal: (i) Evolution of dimensionless capillary pressure calculated as the local curvature $P_c^* = 1/r^*$ in terms of number of step. Red circle marks the critical capillary pressure, where the pressure-driven advancement occurs. Yellow crosses represent the consequent spontaneous events (relaxation). (ii) Conversion from step into time expressed in terms of injected fluid area $A_{inj}^*$ which is normalized by the average pore area. The time for Haines jump is regarded as instantaneous, that is, only the start and end of $P_c^*$ are "felt" at the inlet. The $P_c^*$ values at same invasion progress are marked by the same number in (i) and (ii). (iii) Capillary pressure signal during the whole simulation. The black box is (ii).

size as angularity increases, despite almost constant porosity. For media filled with dodecagons, the average throat size is close to 1, that is, the average throat size is similar to media with perfect spheres, which implies that the shape of dodecagons can be regarded as very close to spherical particles. Figure 4c shows the effective contact angle distribution $\theta$ at the end of displacement (after the final relaxation process when invasion front reaches the boundary) for the case with an intrinsic contact angle $\theta_0 = 120°$. Note that there is one effective contact angle per triple line (and thus two per meniscus). Due to the sharp edge pinning effect, the distribution narrows for grains with decreasing angularity. In the case of perfect spheres, one can expect a single value of $\theta = \theta_0$ according to Equation 1. Therefore, Figures 4b and 4(c) summarize the important influences of particle angularity on pore geometry features and contact angle distribution, which will consequently impact the capillary pressure signal and invasion morphology.

### 3.1. Capillary Pressure Signal

As indicated in Figure 5a, the evolution of dimensionless capillary pressure $P_c^*$ shows larger fluctuations for media with squares compared with more spherical grains (dodecagons), implying greater randomness in local capillary resistance. At the same time, larger mean value is observed with increasing $\theta_0$, which is a direct result of greater curvature of menisci. The distribution of $P_{start}^*$, the avalanches starting pressure, can also be directly obtained from the simulation (Figure 5b), where $P_{start}^*$ is the capillary pressure at pressure-driven event (red circle in Figure 3b(i)). For experiments conducted using spherical glass beads in drainage, $P_{start}^*$ is found to distribute within a relatively narrow region (Furuberg et al., 1996; Måløy et al., 1992; Moura et al., 2020). The $P_{start}^*$ distribution is linked to the total volume capacitance stored in all active menisci (Furuberg et al., 1996), which reflects the characteristics of pore geometry. For spherical grains with given packing structure, the capillary resistance is distinct between "pore" and "throat," leading to the fact that the avalanches are likely to initialize (and finish) at same location and consequently similar $P_{start}^*$. As the shape of particle becomes more angular, the distribution of $P_{start}^*$ widens as a result of increased impact from

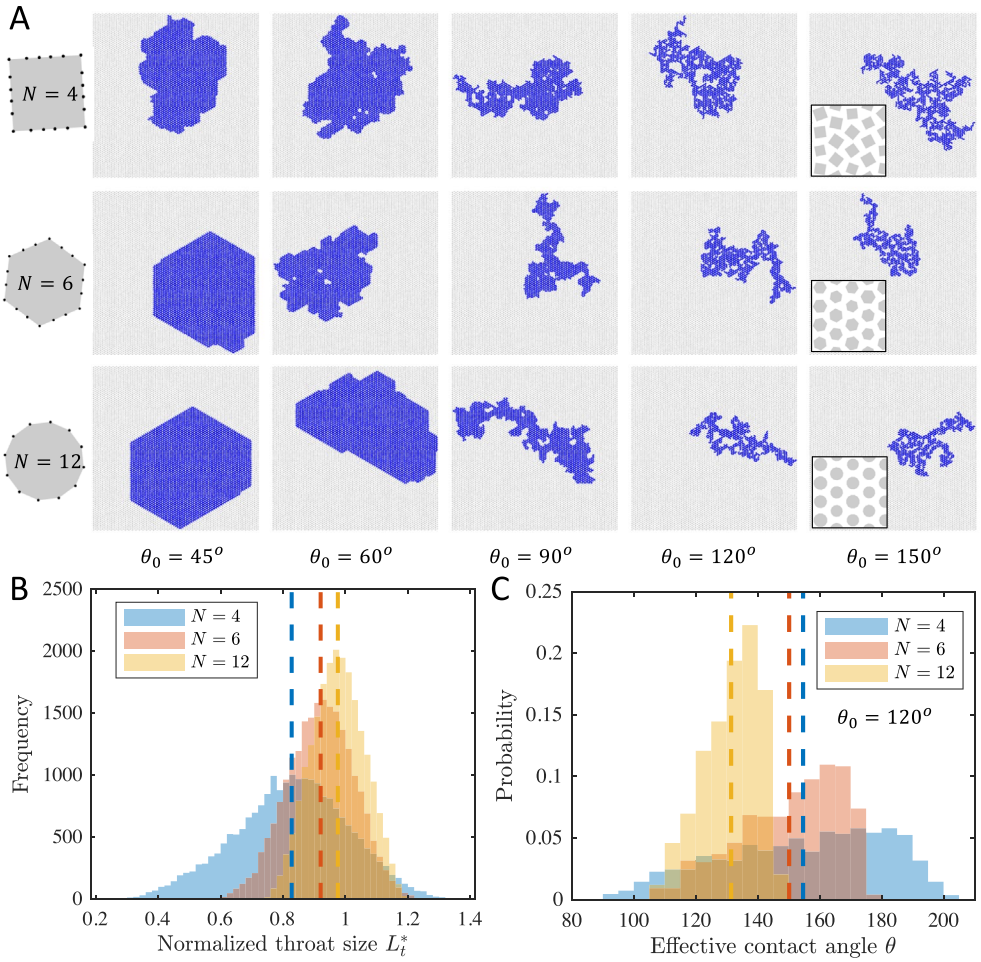


**Figure 4.** (a) Displacement patterns at the end of the simulation for different wettability conditions and grain shapes. Blue color represents the invading fluid injected from the center of domain. Gray color represents grains. Insets in the last column show the typical grain arrangement of a zoomed region. The simulation ends when the invading fluid reaches the boundary. (b) Distribution of normalized throat size for a typical set of porous media of different grain shapes, calculated as the shortest distance between adjacent grains divided by the throat size of volume equivalent spheres. (c) Contact angle distribution of one typical simulation at the end of simulation with an intrinsic contact angle $\theta_0 = 120°$ for different grain shapes. The dashed lines mark the average value for the corresponding data.

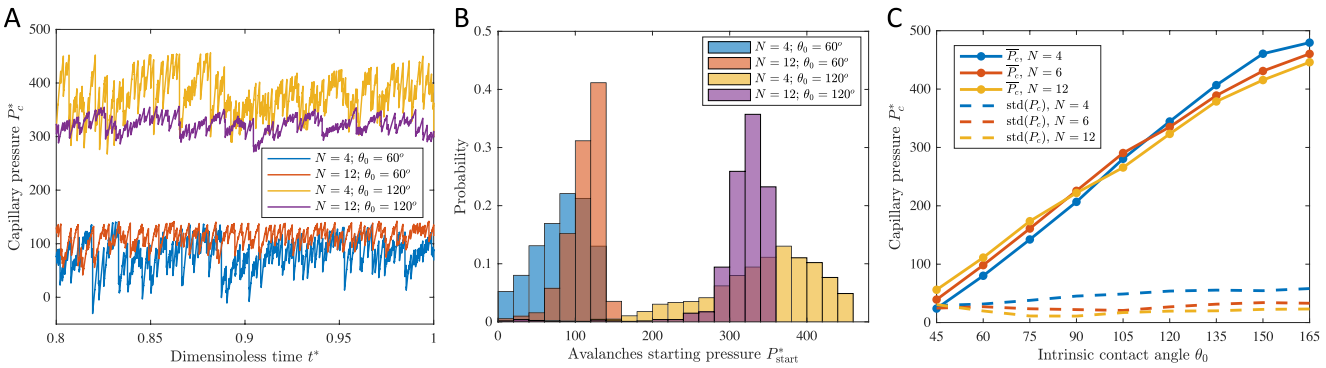


**Figure 5.** (a) Capillary pressure signals $P_c^*$ for media with squares and dodecagons at $\theta_0 = 60°$ and $\theta_0 = 120°$. Only last 20% of invasion is plotted for visualization purpose. (b) Corresponding avalanches starting pressure $P_{start}^*$ distribution for cases in (a), which is the $P_c^*$ at pressure-driven event (red circle in Figure 3b(i)). (c) Mean and standard deviation in $P_c^*$ for all grain shapes and wettability conditions. Values are calculated from five individual simulations.

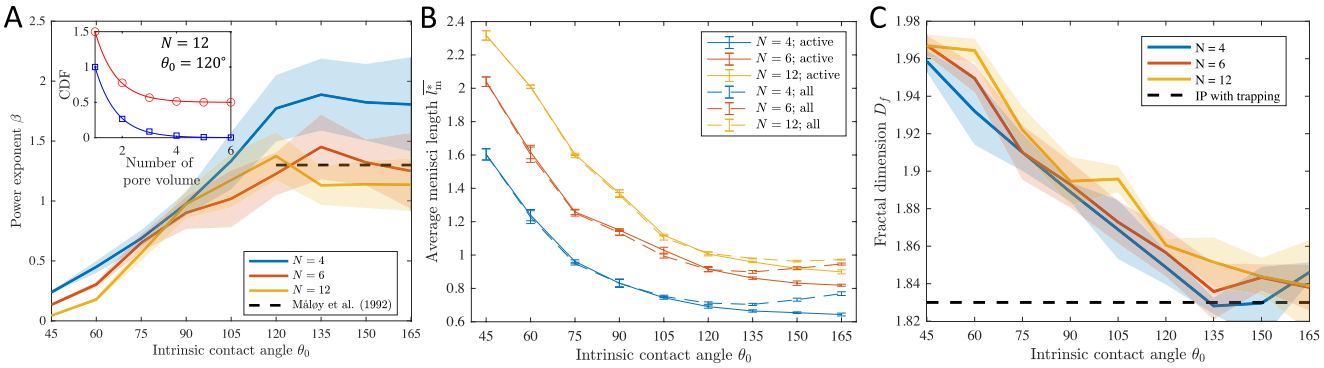


**Figure 6.** (a) Power exponent $\beta$ for different grain shapes and wetting conditions. The black-dashed line is from Måløy et al. (1992) in drainage experiment with glass beads (since the contact angle is not reported, it is assumed that $\theta_0 > 120°$). Inset: Cumulative Haines jump sizes (blue squares) and intervals (red circles) distribution for a typical simulation at $N = 12$ with $\theta_0 = 120°$. The intervals distribution is shifted by 0.5 for visualization purpose. Lines represent exponential fitting with 1.29 and 1.30 for jump sizes and interval sizes, respectively. (b) The normalized average meniscus width $\overline{l_m^*}$ as a function of intrinsic contact angle. Solid (dashed) lines represent values calculated from active (all) menisci. (c) Fractal dimension calculated using the box-counting method as a function of intrinsic contact angle, with shaded area showing the standard deviation of five simulations.

random orientations of grains and pinning of menisci, which is clearly demonstrated in Figure 5b. Figure 5c depicts the mean and standard deviation of $P_c^*$ for all grain shapes and wettability with each value calculated from five individual simulations. As expected, the average capillary pressure increases with increasing contact angle, and the fluctuations in capillary pressure are found to be larger for more angular grains across all wetting conditions. Besides, it can be observed that $\overline{P_c^*}$ is greater (smaller) for angular grains in drainage (imbibition) conditions, with a crossover at around $\theta_0 \approx 90°$, which can be attributed to the change in pore and throat size distribution. It is well understood that the throat (pore) size controls the invasion process in drainage (imbibition). Figure 4c indicates that greater angularity leads to smaller average throat size, and in the meantime greater average pore size (as the porosity is the same), which explains the observed higher capillary pressure in drainage and lower capillary pressure in imbibition.

### 3.2. Haines Jumps and Patterns Characteristics

The size of Haines jump can be obtained as the area filled between two pressure-driven events (shaded area in Figure 1d), where filling events of single and multiple pores are observed. Both the cumulative pressure jump sizes and intervals distributions during drainage experiments have been found to follow an exponential law (Furuberg et al., 1996; Måløy et al., 1992), which is consistent with the simulation results (inset in Figure 6a). The time interval between two jumps is expressed as the injected area of invading fluid, and the area of invading fluid is expressed in terms of number of average pore volume, calculated as the total pore space divided by the number of pores. Note that the distribution of the cumulative intervals is shifted upwards by 0.5 for visualization purpose. The power exponent $\beta$, which is regarded as a signature of the displacement process (Furuberg et al., 1996; Måløy et al., 1992), is plotted for different grain shapes and wetting conditions (Figure 6a). It is shown that $\beta$ increases with the intrinsic contact angle, reaching a plateau at around $\theta_0 = 120°$. Also, in general, the angularity positively correlates with the power exponent. The power exponent $\beta$ from Måløy et al. (1992) in drainage experiment with glass beads is added as black-dashed line for comparison. Since the contact angle was not reported, it is assumed that $\theta_0 > 120°$. Their value of $\beta$ is close to the less angular grains (hexagons and dodecagons), which is consistent with the fact that glass beads are comparatively round and smooth.

The average meniscus width $\overline{l_m^*}$ (or the average throat size where menisci are present), normalized by the throat size of porous medium of same porosity filled with mono-dispersed spheres, can reveal the distribution of menisci sizes for different particle shapes and wetting conditions. Figure 6b shows $\overline{l_m^*}$ as a function of intrinsic contact angle for different angularities with or without consideration of menisci belonging to trapped region. For all active menisci (solid lines), $\overline{l_m^*}$ decreases with increasing $\theta_0$, reflecting stronger stability of pinned meniscus at small throat. Besides, despite constant porosity for all simulations, the average

meniscus size is found to be smaller in angular grains as a result of (i) wider distribution of throat sizes (Figure 4b), and (ii) greater capacity of pinning (upper bound in Equation 1) as the local corner becomes sharper, leading to wider distribution of effective contact angles (Figure 4c). If both active and inactive menisci are considered, however, a non-monotonic relationship is observed. This is a result of incompressibility of the trapped ganglia that prevent the menisci from further advancement and ultimately being pinned at narrower throats. Due to increased amount of trapping at larger contact angle (see Figure 4a), this effect becomes significant at extreme non-wetting condition that leads to increase in $\overline{l_m^*}$. This also implies that the pressure within the trapped ganglia could be lower than the capillary pressure signal measured at the inlet.

To quantify the displacement patterns, the fractal dimension $D_f$, as a measurement of the degree to which a pattern fills space, is calculated using the box-counting method. Figure 6c demonstrates the transition from stable displacement with a $D_f$ of around 1.96 toward the regime of capillary fingering with $D_f \approx 1.84$, which is consistent with previously documented values of 1.96 and 1.83 for compact growth and invasion percolation, respectively (Blunt, 2017; Lenormand & Zarcone, 1989; Primkulov et al., 2018; Trojer et al., 2015; Wilkinson & Willemsen, 1983; Zhao et al., 2016). Furthermore, in spite of considerable variation (standard deviation, represented by the shaded area), an early transition toward capillary fingering, that is, smaller $D_f$ at the same $\theta_0$, can be observed for grains with greater angularity, which confirms the qualitative observation in the displacement patterns in Figure 4a. This could be partially explained by, apart from the variation in local pore structure, the increase of average effective contact angles in angular grains assemblies due to sharp edge pinning effect, which is evident in Figure 4c.

In this study, though we considered simplified particle shapes (regular polygons), more general and complex shapes can be easily implemented by changing the coordinates of grain vertices and updating the local corner angles accordingly. Also, it is possible to consider the viscous effect by incorporating, for example, the recently proposed moving capacitor model (Primkulov et al., 2019). Furthermore, in the current work, the change in distribution of effective contact angle and throat size has been regarded as a direct result of variation in particle shape (Figures 4b and 4c), as simultaneous variations in these two quantities, under fixed porosity, are inevitable with change in particle shape. It could be interesting to solely look at the impact of menisci pinning phenomena at sharp edges by excluding the change in throat (or pore) size distribution, although this would lead to different overall porosity of samples. Note that, for the choice of particle shapes investigated in this study, square grain is chosen as the most angular case instead of triangle. This is because that with current porosity 0.5912, there will be overlaps of grains, if the shape is triangle, when they are randomly rotated. Since the porosity is already relatively large and we do not want to further increase it, also, we try to avoid manually specifying extra criterion during media generation and ensure fully random (homogeneous and isotropic) porous media, the most angular shape for current grain arrangement and porosity without grain overlap is square. On the other hand, dodecagon is used to represent circular grain, as the algorithm is not capable of doing perfect circles since the calculation of critical capillary pressure and advancement of menisci is based on discretization of the grains, and perfect circles correspond to infinite number of mesh points. Nevertheless, it was shown that the case for dodecagon is close to circle, as the average throat size is very close to the porous media filled with perfect circles (Figure 4b).

## 4. Conclusions

In conclusion, we presented the EPONM to probe the effect of grain shapes on quasi-static fluid-fluid displacement in porous media. The model incorporates the mechanisms of pore-scale instabilities (Cieplak & Robbins, 1988, 1990), volume capacitance model (Furuberg et al., 1996; Måløy et al., 1992), and sharp edge pinning effect (Gibbs, 1961; Oliver et al., 1977). This allows us to reproduce the multiphase flow patterns across a wide range of wetting conditions for different grain shapes. The algorithm, with further extension, that is, mainly on geometry description and generalization on determination of instability modes, should be applicable to porous media with arbitrary grain shape/location, such as reconstructed pore geometry from scan of rocks, offering a rigorous approach for investigation of how topological features modify the multiphase displacement in porous media.

At the pore scale, increase in grain angularity not only introduces greater heterogeneity in pore geometry, but also amplifies the effect of menisci pinning at corners. This is directly reflected by the variations in distributions of throat sizes (Figure 4b) and effective contact angles (Figure 4c), which consequently impact both the mean value and fluctuation of the capillary pressure signal (Figure 5a). Macroscopically, an earlier transition from stable displacement toward the regime of capillary fingering is observed both qualitatively from the invasion morphology (Figure 4a) and quantitatively as indicated by the fractal dimension (Figure 6c). Various characteristic metrics have been calculated for comparison with past experimental works, including the distribution of avalanches starting pressure, Haines jump size, and interval. Reasonable agreement is observed, and impacts of grain shape are discussed. In particular, under the condition of same porosity for all studied cases, the average size of menisci is found to be smaller in porous media with angular grains, showing a tendency of pinning at narrower throats as a result of wider distribution of throat sizes (Figure 4b) and greater pinning strength (Equation 1).

Our results have provided independent corroboration of wide distribution of contact angles observed experimentally in mineralogically homogeneous porous media. The profound influences of grain shape are highlighted by systematically analyzing the displacement processes, deepening the understanding of the interplay between pore geometry and wettability. The proposed pore-network model offers an efficient approach for the investigation of multiphase flow in natural porous media.

## Data Availability Statement

Data sets associated with this work are available online (https://doi.org/10.6084/m9.figshare.13369733).

**Acknowledgments**
This work was financially supported by the Australian Research Council (Projects DP170102886) and The University of Sydney SOAR Fellowship. Y. Gan acknowledges the financial support of Labex MMCD (ANR-11-LABX-022-01) for his stay at Laboratoire Navier at ENPC. Z. Wang thanks Ms Zi Ying for fruitful discussion.

## References

AlRatrout, A., Blunt, M. J., & Bijeljic, B. (2018). Wettability in complex porous materials, the mixed-wet state, and its relationship to surface roughness. *Proceedings of the National Academy of Sciences of the United States of America*, *115*(36), 8901–8906. https://doi.org/10.1073/pnas.1803734115

Armstrong, R. T., Georgiadis, A., Ott, H., Klemin, D., & Berg, S. (2014). Critical capillary number: Desaturation studied with fast x-ray computed microtomography. *Geophysical Research Letters*, *41*, 55–60. https://doi.org/10.1002/2013GL058075

Blunt, M., Fayers, F., & Orr, F. M. (1993). Carbon dioxide in enhanced oil recovery. *Energy Conversion and Management*, *34*(9), 1197–1204. (Proceedings of the International Energy Agency Carbon Dioxide Disposal Symposium).

Blunt, M. J. (1998). Physically-based network modeling of multiphase flow in intermediate-wet porous media. *Journal of Petroleum Science and Engineering*, *20*(3), 117–125. https://doi.org/10.1016/S0920-4105(98)00010-2

Blunt, M. J. (2001). Flow in porous media pore-network models and multiphase flow. *Current Opinion in Colloid & Interface Science*, *6*(3), 197–207. https://doi.org/10.1016/S1359-0294(01)00084-X

Blunt, M. J. (2017). *Multiphase flow in permeable media: A pore-scale perspective*. Cambridge University Press. https://doi.org/10.1017/9781316145098

Blunt, M. J., Alhosani, A., Lin, Q., Scanziani, A., & Bijeljic, B. (2021). Determination of contact angles for three-phase flow in porous media using an energy balance. *Journal of Colloid and Interface Science*, *582*, 283–290. https://doi.org/10.1016/j.jcis.2020.07.152

Blunt, M. J., Lin, Q., Akai, T., & Bijeljic, B. (2019). A thermodynamically consistent characterization of wettability in porous media using high-resolution imaging. *Journal of Colloid and Interface Science*, *552*, 59–65. https://doi.org/10.1016/j.jcis.2019.05.026

Cassie, A. B. D., & Baxter, S. (1944). Wettability of porous surfaces. *Transactions of the Faraday Society*, *40*, 546–551. http://dx.doi.org/10.1039/TF9444000546

Chapuis, O., Prat, M., Quintard, M., Chane-Kane, E., Guillot, O., & Mayer, N. (2008). Two-phase flow and evaporation in model fibrous media: Application to the gas diffusion layer of PEM fuel cells. *Journal of Power Sources*, *178*(1), 258–268. https://doi.org/10.1016/j.jpowsour.2007.12.011

Chen, Y.-F., Wu, D.-S., Fang, S., & Hu, R. (2018). Experimental study on two-phase flow in rough fracture: Phase diagram and localized flow channel. *International Journal of Heat and Mass Transfer*, *122*, 1298–1307. https://doi.org/10.1016/j.ijheatmasstransfer.2018.02.031

Cieplak, M., & Robbins, M. O. (1988). Dynamical transition in quasistatic fluid invasion in porous media. *Physical Review Letters*, *60*, 2042–2045. https://doi.org/10.1103/PhysRevLett.60.2042

Cieplak, M., & Robbins, M. O. (1990). Influence of contact angle on quas-istatic fluid invasion of porous media. *Physical Review B: Condensed Matter*, *41*, 11508–11521. https://doi.org/10.1103/PhysRevB.41.11508

Crisp, D. J., & Thorpe, W. H. (1948). The water-protecting properties of insect hairs. *Discussions of the Faraday Society*, *3*, 210–220. http://dx.doi.org/10.1039/DF9480300210

Furuberg, L., Måløy, K. J., & Feder, J. (1996). Intermittent behavior in slow drainage. *Physical Review E - Statistical Physics, Plasmas, Fluids, and Related Interdisciplinary Topics*, *53*, 966–977. https://doi.org/10.1103/PhysRevE.53.966

Gao, N., & Yan, Y. (2009). Modeling superhydrophobic contact angles and wetting transition. *Journal of Bionic Engineering*, *6*(4), 335–340. https://doi.org/10.1016/S1672-6529(08)60135-3

Geistlinger, H., & Zulfiqar, B. (2020). The impact of wettability and surface roughness on fluid displacement and capillary trapping in 2D- and 3D-porous media. Part 1: Wettability-controlled phase transition of trapping efficiency in glass beads packs. *Water Resources Research*, *56*(10), e2019WR026826. https://doi.org/10.1029/2019WR026826

Gibbs, J. W. (1961). *The scientific papers* (Vol. 1). New York, NY: Dover Publications.

Holtzman, R. (2016). Effects of pore-scale disorder on fluid displacement in partially-wettable porous media. *Scientific Reports*, *6*, 36221. https://doi.org/10.1038/srep36221

Holtzman, R., & Segre, E. (2015). Wettability stabilizes fluid invasion into porous media via nonlocal, cooperative pore filling. *Physical Review Letters*, *115*, 164501. https://doi.org/10.1103/PhysRevLett.115.164501

Hu, R., Lan, T., Wei, G.-J., & Chen, Y.-F. (2019). Phase diagram of quasi-static immiscible displacement in disordered porous media. *Journal of Fluid Mechanics*, *875*, 448–475. https://doi.org/10.1017/jfm.2019.504

Ju, Y., Gong, W., Chang, W., & Sun, M. (2020). Effects of pore characteristics on water-oil two-phase displacement in non-homogeneous pore structures: A pore-scale lattice Boltzmann model considering various fluid density ratios. *International Journal of Engineering Science*, *154*, 103343. https://doi.org/10.1016/j.ijengsci.2020.103343

Jung, M., Brinkmann, M., Seemann, R., Hiller, T., Sanchez de La Lama, M., & Herminghaus, S. (2016). Wettability controls slow immiscible displacement through local interfacial instabilities. *Physical Review Fluids*, *1*, 074202. https://doi.org/10.1103/PhysRevFluids.1.074202

Lake, L. W., Johns, R., Rossen, B., & Pope, G. (2014). *Fundamentals of enhanced oil recovery*. Society of Petroleum Engineers.

Lenormand, R. (1990). Liquids in porous media. *Journal of Physics: Condensed Matter*, *2*(S), SA79–SA88. https://doi.org/10.1088/0953-8984/2/s/008

Lenormand, R., Touboul, E., & Zarcone, C. (1988). Numerical models and experiments on immiscible displacements in porous media. *Journal of Fluid Mechanics*, *189*, 165–187. https://doi.org/10.1017/s0022112088000953

Lenormand, R., & Zarcone, C. (1989). Capillary fingering: Percolation and fractal dimension. *Transport in Porous Media*, *4*(6), 599–612. https://doi.org/10.1007/BF00223630

Lipiec, J., Ku, J., Slowiska-Jurkiewicz, A., & Nosalewicz, A. (2006). Soil porosity and water infiltration as influenced by tillage methods. *Soil and Tillage Research*, *89*(2), 210–220. https://doi.org/10.1016/j.still.2005.07.012

Måløy, K. J., Furuberg, L., Feder, J., & Jøssang, T. (1992). Dynamics of slow drainage in porous media. *Physical Review Letters*, *68*, 2161–2164. https://doi.org/10.1103/PhysRevLett.68.2161

Marmur, A. (2003). Wetting on hydrophobic rough surfaces: To be heterogeneous or not to be? *Langmuir*, *19*(20), 8343–8348. https://doi.org/10.1021/la0344682

Mason, G., & Morrow, N. R. (1994). Effect of contact angle on capillary displacement curvatures in pore throats formed by spheres. *Journal of Colloid and Interface Science*, *168*(1), 130–141. https://doi.org/10.1006/jcis.1994.1402

Matter, J. M., Stute, M., Snæbjörnsdottir, S. Ó., Oelkers, E. H., Gislason, S. R., Aradottir, E. S., et al (2016). Rapid carbon mineralization for permanent disposal of anthropogenic carbon dioxide emissions. *Science*, *352*(6291), 1312–1314. https://doi.org/10.1126/science.aad8132

Mehmani, A., Kelly, S., Torres-Verdn, C., & Balhoff, M. (2019). Residual oil saturation following gas injection in sandstones: Microfluidic quantification of the impact of pore-scale surface roughness. *Fuel*, *251*, 147–161. https://doi.org/10.1016/j.fuel.2019.02.118

Mishra, H., Schrader, A. M., Lee, D. W., Gallo, A., Chen, S.-Y., Kaufman, Y., et al. (2016). Time-dependent wetting behavior of PDMS surfaces with bioinspired, hierarchical structures. *ACS Applied Materials & Interfaces*, *8*(12), 8168–8174. https://doi.org/10.1021/acsami.5b10721

Moulinet, S., & Bartolo, D. (2007). Life and death of a fakir droplet: Impalement transitions on superhydrophobic surfaces. *The European Physical Journal E*, *24*(3), 251–260. https://doi.org/10.1140/epje/i2007-10235-y

Moura, M., Mly, K. J., Flekky, E. G., & Toussaint, R. (2020). Intermittent dynamics of slow drainage experiments in porous media: Characterization under different boundary conditions. *Frontiers in Physics*, *7*(217). 10.3389/fphy.2019.00217

Nadim, F., Hoag, G. E., Liu, S., Carley, R. J., & Zack, P. (2000). Detection and remediation of soil and aquifer systems contaminated with petroleum products: An overview. *Journal of Petroleum Science and Engineering*, *26*(1), 169–178.

Oliver, J., Huh, C., & Mason, S. (1977). Resistance to spreading of liquids by sharp edges. *Journal of Colloid and Interface Science*, *59*(3), 568–581. https://doi.org/10.1016/0021-9797(77)90052-2

Papadopoulos, P., Mammen, L., Deng, X., Vollmer, D., & Butt, H.-J. (2013). How superhydrophobicity breaks down. *Proceedings of the National Academy of Sciences of the United States of America*, *110*(9), 3254–3258. https://doi.org/10.1073/pnas.1218673110

Primkulov, B. K., Pahlavan, A. A., Fu, X., Zhao, B., MacMinn, C. W., & Juanes, R. (2019). Signatures of fluid-fluid displacement in porous media: Wettability, patterns and pressures. *Journal of Fluid Mechanics*, *875*, R4. https://doi.org/10.1017/jfm.2019.554

Primkulov, B. K., Talman, S., Khaleghi, K., Rangriz Shokri, A., Chalaturnyk, R., Zhao, B., et al. (2018). Quasistatic fluid-fluid displacement in porous media: Invasion-percolation through a wetting transition. *Physical Review Fluids*, *3*, 104001. https://doi.org/10.1103/PhysRevFluids.3.104001

Purcell, W. (1950). Interpretation of capillary pressure data. *Journal of Petroleum Technology*, *2*(08), 11–12. https://doi.org/10.2118/950369-G

Rabbani, H. S., Or, D., Liu, Y., Lai, C.-Y., Lu, N. B., Datta, S. S., et al. (2018). Suppressing viscous fingering in structured porous media. *Proceedings of the National Academy of Sciences of the United States of America*, *115*, 4833–4838. https://doi.org/10.1073/pnas.1800729115

Ran, H., Jiamin, W., Zhibing, Y., Yi-Feng, C., & Tetsu, T. (2018). Wettability and flow rate impacts on immiscible displacement: A theoretical model. *Geophysical Research Letters*, *45*(7), 3077–3086. https://doi.org/10.1002/2017GL076600

Sbragaglia, M., Peters, A. M., Pirat, C., Borkent, B. M., Lammertink, R. G. H., Wessling, M., & Lohse, D. (2007). Spontaneous breakdown of superhydrophobicity. *Physical Review Letters*, *99*, 156001. https://doi.org/10.1103/PhysRevLett.99.156001

Seo, D., Schrader, A. M., Chen, S.-Y., Kaufman, Y., Cristiani, T. R., Page, S. H., et al. (2018). Rates of cavity filling by liquids. *Proceedings of the National Academy of Sciences of the United States of America*, *115*(32), 8070–8075. https://doi.org/10.1073/pnas.1804437115

Szulczewski, M. L., MacMinn, C. W., Herzog, H. J., & Juanes, R. (2012). Lifetime of carbon capture and storage as a climate-change mitigation technology. *Proceedings of the National Academy of Sciences of the United States of America*, *109*(14), 5185–5189. https://doi.org/10.1073/pnas.1115347109

Trojer, M., Szulczewski, M. L., & Juanes, R. (2015). Stabilizing fluid-fluid displacements in porous media through wettability alteration. *Physical Review Applied*, *3*, 054008. https://doi.org/10.1103/PhysRevApplied.3.054008

Wang, Z., Chauhan, K., Pereira, J.-M., & Gan, Y. (2019). Disorder characterization of porous media and its effect on fluid displacement. *Physical Review Fluids*, *4*, 034305. https://doi.org/10.1103/PhysRevFluids.4.034305

Wang, Z., Pereira, J.-M., & Gan, Y. (2020). Effect of wetting transition during multiphase displacement in porous media. *Langmuir*, *36*(9), 2449–2458. https://doi.org/10.1021/acs.langmuir.9b03780

Wenzel, R. N. (1936). Resistance of solid surfaces to wetting by water. *Industrial & Engineering Chemistry*, *28*(8), 988–994. https://doi.org/10.1021/ie50320a024

Wilkinson, D., & Willemsen, J. F. (1983). Invasion percolation: A new form of percolation theory. *Journal of Physics A: Mathematical and General*, *16*(14), 3365–3376. https://doi.org/10.1088/0305-4470/16/14/028

Xu, W., Ok, J. T., Xiao, F., Neeves, K. B., & Yin, X. (2014). Effect of pore geometry and interfacial tension on water-oil displacement efficiency in oil-wet microfluidic porous media analogs. *Physics of Fluids*, *26*(9), 093102. https://doi.org/10.1063/1.4894071

Yortsos, Y. C., Xu, B., & Salin, D. (1997). Phase diagram of fully developed drainage in porous media. *Physical Review Letters*, *79*, 4581–4584. https://doi.org/10.1103/PhysRevLett.79.4581

Zhao, B., MacMinn, C. W., & Juanes, R. (2016). Wettability control on multiphase flow in patterned microfluidics. *Proceedings of the National Academy of Sciences of the United States of America*, *113*(37), 10251–10256. https://doi.org/10.1073/pnas.1603387113

Zulfiqar, B., Vogel, H., Ding, Y., Golmohammadi, S., Kchler, M., Reuter, D., & Geistlinger, H. (2020). The impact of wettability and surface roughness on fluid displacement and capillary trapping in 2D- and 3D-porous media: Part 2: Combined effect of wettability, surface roughness, and pore space structure on trapping efficiency in sand packs and micromodels. *Water Resources Research*, *56*(10), e2020WR027965. https://doi.org/10.1029/2020WR027965